High-Pressure Structural and Thermodynamic Properties of Cerium Orthosilicates ($CeSiO_4$)

Andrew Strzelecki, Xiaodong Zhao, Jason Baker, Paul Estevenon, Thomas Barral, Adel Mesbah, Dmitry Popov, Stella Chariton, Vitali Prakapenka, Sohan Ahmed, et al.

THE JOURNAL OF PHYSICAL CHEMISTRY C
A JOURNAL OF THE AMERICAN CHEMICAL SOCIETY

pubs.acs.org/JPCC

Article

High-Pressure Structural and Thermodynamic Properties of Cerium Orthosilicates ($CeSiO_4$)

Published as part of The Journal of Physical Chemistry virtual special issue "Early-Career and Emerging Researchers in Physical Chemistry Volume 2".

Andrew Strzelecki, Xiaodong Zhao, Jason Baker, Paul Estevenon, Thomas Barral, Adel Mesbah, Dmitry Popov, Stella Chariton, Vitali Prakapenka, Sohan Ahmed, Choong-Shik Yoo, Nicolas Dacheux, Hongwu Xu, and Xiaofeng Guo*

Cite This: https://doi.org/10.1021/acs.jpcc.2c06657

Read Online

ACCESS | Metrics & More | Article Recommendations | Supporting Information

ABSTRACT: Pressure-induced phase transitions from the zircon structure-type ($I4_1/amd$) to the scheelite structure type ($I4_1/a$) are known for many ternary oxides systems (ABO_4). In this work, we present the first high-pressure study on synthetic stetindite ($CeSiO_4$) by a combination of in situ high-pressure synchrotron powder X-ray diffraction up to 36 GPa, implemented with and without dual sided laser heating, and in situ high-pressure Raman spectroscopy up to 43 GPa. Two phase transitions were identified: zircon to a high-pressure low-symmetry (HPLS) phase at 15 GPa and then to a scheelite at 18 GPa. The latter from HPLS scheelite phase was found irreversible; i.e., scheelite is fully quenchable at ambient conditions, as in other zircon-type phases. The bulk moduli (K_0) of stetindite, HPLS, and high-pressure scheelite phases were determined respectively as 171(5), 105(4), and 221(40) GPa by fitting to a second-order Birch−Murnaghan equation of state The pressure derivatives of vibrational modes and Grüneisen parameters of the zircon-structured polymorph is similar to those of other orthosilicate minerals. Due to the larger ionic radii of Ce^{4+}, with respect to Zr^{4+}, stetindite was found to possess a softer bulk modulus and undergo the phase transitions at a lower pressure than zircon ($ZrSiO_4$),;such observations are consistent with what were found with coffinite ($USiO_4$).

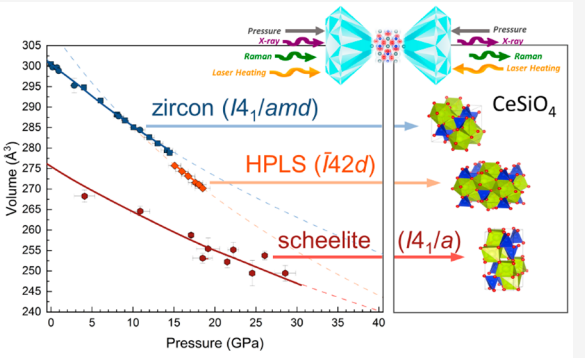

1. INTRODUCTION

Pressure-induced phase transitions from the zircon structure-type (space group: $I4_1/amd$) to the scheelite structure-type (space group: $I4_1/a$) are known for many different ternary oxides (ABO_4).[1,2] These ABO_4 systems include orthosilicates ($ZrSiO_4$, $HfSiO_4$ and $USiO_4$),[3−9] heavy rare earth element (HREE) orthophosphates ($HREEPO_4$),[10−14] and rare earth element (REE) orthovanadates ($REEVO_4$).[15−21] The most studied of these phases is the eponymous orthosilicate mineral, zircon ($ZrSiO_4$), which undergoes a phase transition between 20 and 30 GPa, depending on the composition of natural samples used (i.e., concentrations of Hf, U, or REE) and degree of metamictization.[3−6,22−28] This high-pressure phase of $ZrSiO_4$ has been identified in natural systems such as the ejecta associated with meteorite impacts and was given a mineral name, reidite (scheelite structure type; space group: $I4_1/a$).[29] The pressure-induced phase transition from zircon to reidite results in an approximately 10% increase in the overall density, with the [001] channels of zircon being completely eliminated in reidite (Figure 1).[2,30] More recently, an intermediate phase between zircon and reidite has been reported to occur between 20 and 25 GPa.[22,31] This new high-pressure polymorph has been referred to a high-pressure low-symmetry (HPLS) phase (space group: $I\bar{4}_2d$), resulting from slight rotation and twisting of the SiO_4 and MO_8 polyhedra in the zircon structure (Figure 1).[22,31]

Studying high-pressure transitions of zircon-type materials also has important thermophysical implications for their applications. Materials possessing the zircon structure tend to have low chemical reactivity, low solubility, and good resistance to radiation damage, which make them ideal candidates for ceramic based waste hosts for the permanent immobilization of actinides from nuclear wastes.[32−37] In particular the use of zircon has been proposed for the disposal of plutonium (Pu) associated with the defense program since

Received: September 18, 2022
Revised: January 3, 2023

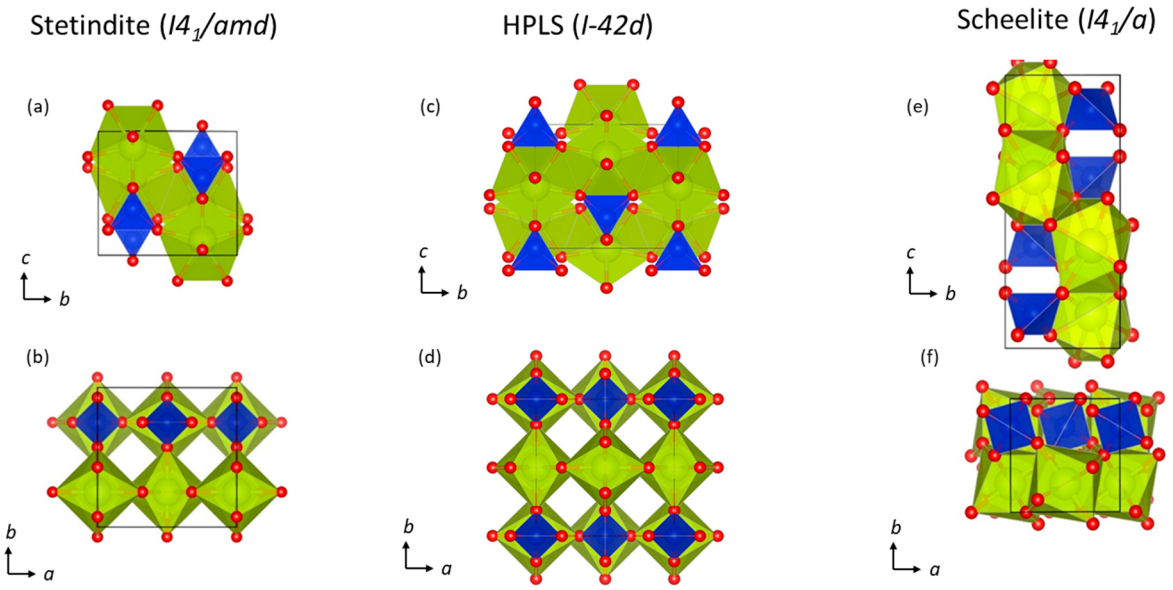

Figure 1. Crystal structures of the low-pressure stetindite phase ($I4_1/amd$), the intermediate-pressure HPLS phase ($I\bar{4}_2d$), and the high-pressure scheelite phase ($I4_1/a$). (a, c, e) Projected along the *a*-axis. (b, d, f) Projected along the *c*-axis..

the 1990s.[38] Studying the thermochemical and thermophysical properties of ceramic waste hosts is paramount in order to confidently model and predict their long-term behavior during storage.[38−46] However, synthesizing the $PuSiO_4$ phase is difficult.[47,48] Thus, examining Pu-surrogate silicate is a rational approach to understand material behaviors and properties of $PuSiO_4$. Because the ionic radius of Ce^{4+} (0.97 Å) is similar to that of Pu^{4+} (0.96 Å) in an 8-fold coordination environment,[49] equivalent to the MO_8 snub-disphenoid of the zircon structure-type, Ce is an effective surrogate for approximating the solid state behavior of Pu.[50−53] Ce can be incorporated in the zircon structure and form pure phase $CeSiO_4$, with its natural occurrence, stetindite, discovered in Norway in 2009.[54] However, no high-pressure (high-*P*) studies have been reported for stetindite, partly because stetindite is also very difficult to synthesize.[55,56] The advent of synthetic stetindite has allowed for several recent studies to investigate some of its thermochemical[57,58] and thermophysical properties.[59] In this work, we continue to study the thermophysical properties of synthetic stetindite by examining its structural behavior under high pressures as determined by a combination of in situ high-pressure synchrotron powder X-ray diffraction up to 36 GPa, implemented with and without dual sided laser heating, and in situ high-pressure Raman spectroscopy up to 43 GPa.

2. EXPERIMENTAL METHODS

2.1. Sample Synthesis. Two batches of synthetic stetindite ($CeSiO_4$) were prepared in this study. Each batch was synthesized hydrothermally, in accordance to the protocol described by Estevenon et al.,[56] in which a Ce^{3+}-silicate solid precursor (A-$Ce_2Si_2O_7$) was used. A-$Ce_2Si_2O_7$ was synthesized by solid state route, in which a stoichiometric mixture of CeO_2 (Sigma-Aldrich; particle size < 5 μm) and SiO_2 (Sigma-Aldrich, 10−20 nm) were mechanically milled (30 Hz, 1 h) in a Retsch MM 200 vibration mill mixer using a tungsten carbide milling vessel. The resulting mixture was pelletized by uniaxial pressing under 5 MPa at room temperature and then heated at 1350 °C under a reducing atmosphere (Ar−4% H_2) to produce A-$Ce_2Si_2O_7$. 200 mg of the Ce^{3+}-silicate solid precursor was then placed in contact with 4 mL of a 0.75 M HNO_3 solution (prepared by dilution of ACS grade 70% HNO_3, Sigma-Aldrich). In the synthesis of the first batch of $CeSiO_4$ (later used in in situ high-pressure synchrotron XRD with Ne as a pressure transmitting medium, PTM), the acidity of the solution was adjusted to a pH of 7.0 ± 0.1 with a freshly prepared NaOH solution (from ACS grade NaOH pellets, Sigma-Aldrich). In the second batch of $CeSiO_4$ (later used in the in situ high-pressure laser-heated synchrotron XRD experiment in which KCl was used as the PTM), the acidity of the solution was adjusted to a pH 6.5 ± 0.1, again with a freshly prepared NaOH solution (from ACS grade NaOH pellets, Sigma-Aldrich). Moreover, in the second batch, an excess of 8 mol % Si was added to the mixture (8.8 mg of $Na_2SiO_3{\cdot}5H_2O$) to avoid the CeO_2 formation. In both batches, the mixtures were then hydrothermally treated for 7 days at 150 °C under air atmosphere using a Parr autoclave. The final products were separated from the supernatant solution by centrifugation, washed twice with deionized water and once with ethanol, and then finally dried overnight at 60 °C. The final products of both synthetic routes lead to single phased $CeSiO_4$ of high crystallinity.[56,57,59]

2.2. In Situ High-Pressure Synchrotron XRD. The pressure generated in this study was done through a Princeton-type symmetric DAC. The sample was loaded in a laser-drilled hole (150 μm diameter) at the center of a pre-indented (45 μm thickness) steel gasket, which was encapsulated between two diamonds (culet size: 300 μm). The gasket was drilled using the High-Pressure Collaborative Access Team (HPCAT) laser drilling system at the Advanced Photon Source (APS), Argonne National Laboratory (ANL).[60] Two ruby spheres were placed into the sample cavity as the pressure calibrant. Pressure was obtained by using the standard ruby pressure scale based on a pressure-induced shift of the R_1 fluorescence line of ruby, measured by an online fluorescence spectrometer system, which employs a 532 nm laser.[61,62] Ne gas was used as the PTM and was loaded using the GeoSoilEnviroCARS (GSECARS) gas loading system at APS, ANL to an initial pressure of 4.0 ± 0.2 GPa.[63] The loaded DAC was then

https://doi.org/10.1021/acs.jpcc.2c06657
J. Phys. Chem. C XXXX, XXX, XXX−XXX

transferred to the HPCAT beamline 16-BM-D at APS, ANL, where in situ high-pressure XRD measurements were conducted. The X-ray wavelength used was 0.4133 Å (30 keV), with a beam size of 5 × 5 μm^2. Two-dimensional (2D) diffraction images were collected using a Mar 345 detector, and the geometric parameters were calibrated using a CeO_2 standard. The sample to detector distance was fixed at 299.5 mm. All collected two-dimensional images were calibrated, masked, and integrated through the use of Dioptas.[64] The obtained XRD patterns of stetindite and high-pressure phases were analyzed through Rietveld method using the General Structure Analysis System software version II (GSAS-II).[65] The background was modeled by the Chebyshev function. The structure reported in Strzelecki et al.[59] for stetindite at room temperature served as the starting structural model for the refinements of phases under low pressures, the structure reported by Stangarone et al.[22] for HPLS zircon served as the starting structural model for the refinements of the intermediate-pressure phase, and the structure reported for high-pressure phase of coffinite ($USiO_4$) by Zhang et al.[7] served as the starting model for the refinements for scheelite phase.

2.3. In Situ High-Pressure Laser-Heated Synchrotron XRD. The sample and a small piece of Pt powder were placed between two KCl plates. Because KCl is hydroscopic, which can alter the hydrostatic conditions of the experiment,[66] it was dried at 723 K for 24 h prior to being loaded (and was stored in a 373 K drying oven when not in use). KCl was used as the PTM, thermal insulator, and internal pressure marker, and Pt as a laser coupler and a secondary pressure maker. Such a "sandwich" layered mixture was loaded into an electric discharge machine (EDM) drilled hole (150 μm diameter) at the center of a preiindented (35 μm thickness) Re gasket. The loaded DAC was then transferred to the GSECARS beamline 13-ID-D at APS, ANL, where in situ high-pressure and high-temperature XRD measurements were conducted. The pressure generated in this study was done through the same Princeton-type symmetric DAC (culet size: 300 μm) used in the high-pressure synchrotron XRD experiment described above. High temperatures were generated by using the on-site double-sided laser heating system.[67,68] The laser beam was aligned coaxially with the X-ray beam to measure diffraction patterns on the heating spot. The typical beam diameters for the laser heating spots were 10−20 μm. The temperatures generated during the laser heating was determined spectroradiometerically using the gray-body approximation.[66,69] The X-rays had a wavelength of 0.3344 Å (37 keV), with a beam size of ~2.5 × 2.5 μm. The beam geometric parameters were calibrated using LaB_6. The distance from sample to detector was fixed at 236.7 mm. The two-dimensional (2D) images were collected utilizing a Pilatus CdTe area detector. All collected two-dimensional images were calibrated, masked, and integrated through the use of Dioptas.[64] The Rietveld refinement on the obtained XRD data were the same as the description in Section 2.2. Based on the pressure−volume equation of state (EOS) of KCl-B1 (space group: $Fm\bar{3}m$) and KCl-B2 (space group: $Pm\bar{3}m$) reported by Dewaele et al.,[70] and the pressure−volume EOS for Pt (space group: $Fm\bar{3}m$) reported by Zha et al.,[71] the pressure in the cell was reported by taking the average of the two derived pressures with the error as two standard deviations of the mean.

2.4. In Situ High-Pressure Raman Spectroscopy. Raman spectroscopic measurements were performed using a Horiba LabRAM HR Evolution Raman spectrometer/microscope system of the Radiogeochemistry Team at Los Alamos National Laboratory (LANL).[72,73] A 532 nm laser was utilized for the spectroscopic measurements, and an Olympus 20× long-working-distance objective lens was used to visualize the sample and focus the laser into the sample chamber. All spectra were collected in the 100−1400 cm^{-1} range. The maximum laser output is 100 mW but is greatly attenuated before interacting with the sample. The system is equipped with an 1800 gr/mm which yields an effective resolution of 0.33 cm^{-1}. The collected spectra were corrected by subtracting the background and were fitted using a Lorentz-type function. For the in situ high-pressure Raman spectroscopic measurements, a Princeton-style symmetric DAC with Type IIb, ultralow fluorescence 300 μm culet diamonds (Almax) were used to generate high pressure. The sample was loaded in a drilled hole (125 μm diameter) at the center of a pre-indented (50 μm thickness) stainless-steel gasket. Two ruby microspheres were placed into the sample cavity as the pressure calibrant. The PTM used was a 4:1 methanol: ethanol mixture. The sample was compressed from room pressure up to 43.3 ± 2.2 GPa, and Raman spectra were collected on both compression and decompression. In addition, the sample recovered after the in situ high $P-T$ synchrotron XRD was also analyzed by Raman spectroscopy after being removed from the DAC. This was done by placing the recovered gasket onto a glass slide.

3. RESULTS

3.1. In Situ High-Pressure Synchrotron XRD. Powder X-ray diffraction patterns at various pressures during compression and decompression are shown in Supporting Information Figure S1. Figure S2 shows representative fitted patterns of $CeSiO_4$ at 4.0 ± 0.2, 15.1 ± 0.8, and 36.0 ± 1.8 GPa. During compression at room temperature, stetindite was stable up to 14.5 ± 0.7 GPa, at which point it began to transform to HPLS (Figure S1). The HPLS phase persisted from 15.1 ± 0.8 to 18.5 ± 0.9 GPa, above which it began to convert to scheelite. The phase transition to scheelite was complete at 29.9 ± 1.5 GPa, in which no more reflections attributed to the HPLS structure could be found (Figure S1). The scheelite structure was found to persist when the sample was decompressed to the lowest pressure possibly achieved, 14.7 ± 0.7 GPa. Refinements for stetindite from 4.0 ± 0.2 to 14.5 ± 0.7 GPa yielded R_{wp} values between 0.895% and 0.997% (Table S1). Refinements performed on the HPLS phase from 15.1 ± 0.8 to 18.5 ± 0.9 GPa yielded R_{wp} values between 0.927% and 1.12% (Table S2). Refinements of high-pressure phases from 33.0 ± 1.7 to 36.0 ± 1.8 GPa during compression and all phases during decompression yielded R_{wp} values between 1.25% and 1.41% (Table S3). Rietveld analyses of the XRD patterns at high pressures were difficult because of the broad diffraction peaks caused by the deviatoric stresses (Figure S1).[74]

In addition to the silicate phases, there was a presence of a low diffuse peak around 8° (2θ), possibly attributing to the (200) reflection of ice-(VI),[75] shown in Figure S2a, which was observed during the compression from 4.0 ± 0.2 to 18.5 ± 0.9 GPa. While the presence of ice-(VI) is not consistent with the phase diagram of water,[76,77] it is the only likely phase which would attribute a diffraction peak at the two-theta range it is observed. Other phases that were considered, but did fit the

https://doi.org/10.1021/acs.jpcc.2c06657
J. Phys. Chem. C XXXX, XXX, XXX−XXX

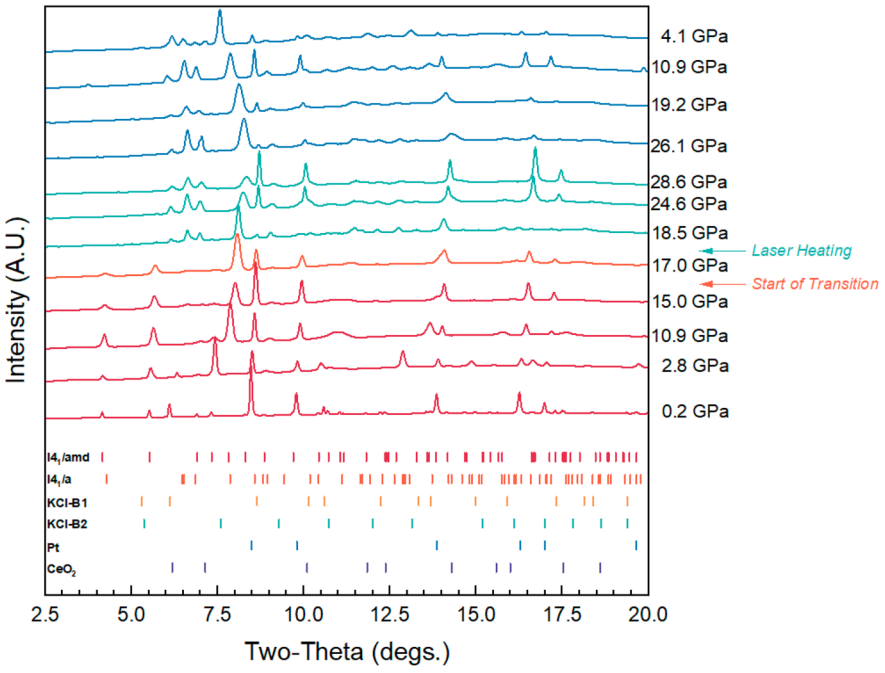

Figure 2. Selected powder X-ray diffraction patterns of $CeSiO_4$ at high pressures. From bottom to top, the patterns were collected during the increase of pressure up to 28.6 GPa. The cell was laser heated at a pressure of 17.0 GPa. The ticks above the *x*-axis indicate the positions of allowed diffraction maxima.

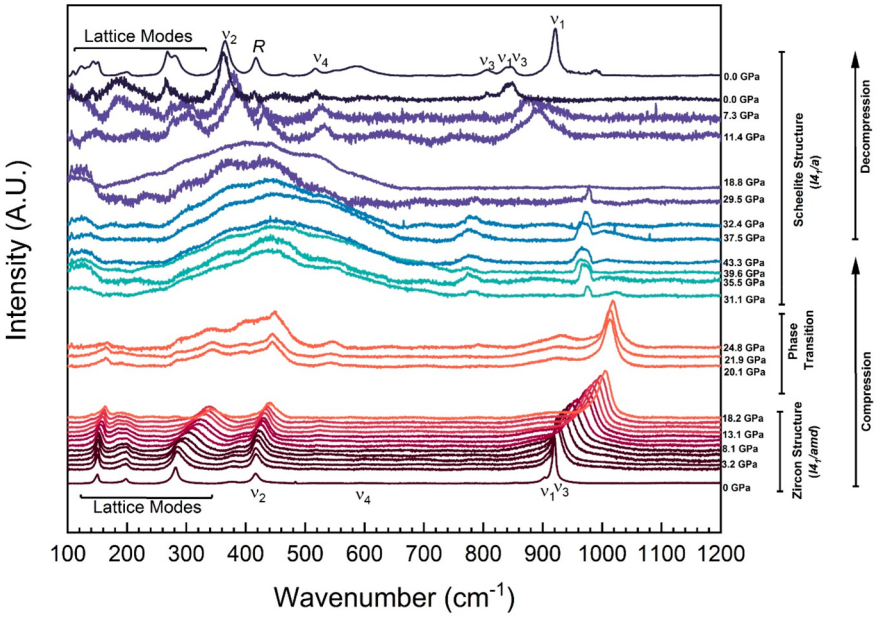

Figure 3. Raman spectra of $CeSiO_4$ at ambient conditions and in situ high pressures up to 43.3 GPa and then decompressed back to ambient conditions. The spectrum presented at the top of the figure was collected on the sample recovered after being compressed and laser heated at beamline 13-ID-D (APS).

measured patterns, were CeO_2, SiO_2 (*α*-quartz and coesite), Al_2O_3, Fe, Ne, as well as ice-(VII). The presence of this extra reflection was not related to the scheelite transition because its occurrence was below transitions of any known zircon-structured orthosilicate at ambient temperature,[4,6−9] while also well within the hydrostatic limit of Ne, ruling out the possibility of an early phase transition due to a steep pressure gradient.[74] Previously, our work has shown that stetindite can retain significant amounts of water (~0.5 mol) as both adsorbed surface water and confined water in the [001] channels of the zircon structure.[57,59] Thus, it is possible that water crystallizes to ice-(VI) upon compression,[78] which has been widely seen in other minerals and materials, such as more porous zeolites.[79] Because the (200) reflections would correspond to a *d*-spacing of 2.988(7) Å, it is possible that such ice-(VI) crystallized from the confined water within the [001] channel. So, the existence of ice-(VI) is also possible by that within the [001] channel the H_2O experiences a lowered pressure due to capillary pressure effect. The other possibility is that the water−ice transition is still taking place within the

https://doi.org/10.1021/acs.jpcc.2c06657
J. Phys. Chem. C XXXX, XXX, XXX−XXX

channel and that really limits the possibility of forming the disordered ice (VII),[80] as confined ice will have different thermodynamic equilibrium than that of bulk ice. However, the extra reflection was excluded from the refinements by means of the exclude function in GSAS-II[65] and consequently was not considered during the whole pattern refinements.

3.2. In Situ High-Pressure Laser-Heated Synchrotron XRD. Powder X-ray diffraction patterns from high $P-T$ XRD are shown in Figure 2, with a representative fitting shown in Figure S3. With KCl as the PTM, stetindite was stable up to 15.0 ± 0.9 GPa (Figure 2). This was evident by the appearance of peaks located at 6.654° corresponding to the (112) diffraction plane of the scheelite-structured phase (Figure S4). The sample was further compressed to 17.0 ± 1.6 GPa (after scheelite transition) and was then subjected to double-sided laser heating (Figure 2). Laser heating provided energy to overcome the kinetic hindrance of the zircon−scheelite transformation and relax any accumulated stresses. This is clearly observed by the sharpness in the diffraction peaks (Figure 2), in contrast to those shown in Figure S2. Note that laser heating was not done to map out the P−V-T EOS. The maximum temperature achieved by the present laser heating setup was estimated to be higher than 3000 K. The exact temperature was not able to be determined as a large flash of the laser saturated the detector. Upon laser quenching, well-crystallized scheelite with minor amounts of CeO_2 were found. CeO_2 may be resulted from thermal decomposition of $CeSiO_4$, which is not thermodynamically favorable with respect to its binary oxides under the standard condition.[57] The cell was then compressed to maximum pressure of 28.6 ± 1.3 GPa, where no further phase transformations were observed (i.e., monazite or fergusonite).[81] During decompression, pressure was lowered to 4.1 ± 1.3 GPa, and the scheelite structure persisted (Figure 2). The resulting Rietveld refinements on the collected patterns yielded R_{wp} values between 1.80% and 7.91% (Tables S4 and S5).

3.3. In Situ High-Pressure Raman Spectroscopy. Collected Raman spectra of $CeSiO_4$ during the compression from ambient to 43.3 ± 2.2 GPa and decompressed back to ambient are displayed in Figure 3. At room temperature, stetindite was stable up to 18.1 ± 0.9 GPa, in agreement with to the results obtained from XRD. The phase transition to scheelite was completed above 24.8 ± 1.2 GPa, above of which no more vibration could be attributed to the zircon structure. The scheelite phase was also fully quenchable upon decompression to ambient conditions. Peaks above 31.1 ± 1.6 GPa became very broad, with all but two of the vibrational modes being easily distinguished. Upon decompression, the broadness of vibrational modes diminished, indicating that the broadness of them was likely due to the deviatoric stress as the result of the 4:1 methanol: ethanol PTM reaching its hydrostatic limit[74] and only partially due to amorphization.[9]

Theoretically, the $I4_1/amd$ space group has 17 Raman-active vibrational modes belonging to the D_{4h} point group.[82−84] Among these 17 modes, nine ($\Gamma_{int} = 2A_{1g} + 2B_{1g} + B_{2g} + 2E_g$)[82,84] can be assigned to the internal vibrations (or normal modes) of the SiO_4 tetrahedron, and the remaining eight ($\Gamma_{ext} = 2B_{1g} + 3E_g$)[82,84] assigned to the external vibrations (lattice modes).[82,84,85] The vibrational modes labeled as ν_1, ν_2, ν_3, and ν_4 correspond to the internal vibrations, where ν_1 (A_{1g}) and ν_3 (B_{1g}) correspond to the symmetric and antisymmetric stretching motions, respectively, and ν_2 (A_{1g}) and ν_4 (B_{1g}) correspond to the symmetric and antisymmetric bending modes, respectively.[86] The motion of the external modes can be further be classified into rotational (E_g) and translational ($B_g + E_g$) modes.[82,86] At ambient conditions, the three external modes appear at 282, 197, and 150 cm^{-1}. Using the assignments of isostructural compounds reported in Syme et al. for $ThSiO_4$ and $ZrSiO_4$,[87] as well as the assignments presented in Mihailova et al.[31] and Stangarone et al. for $ZriSO_4$,[22] the vibrational bands can be described by 282 cm^{-1} (E_g), 197 cm^{-1} (E_g), and 150 cm^{-1} (B_{1g}).[9,22,31] To differentiate between the two external modes, which have identical Mulliken symbols, we adopted the notation of Stangarone et al.,[22] so the vibrational band found at 197 cm^{-1} is E_g (1) and that found at 282 cm^{-1} is E_g (2). The B_g and E_g (2) external vibrational modes are translational external modes whereas the E_g (1) external vibrational mode is a rotational external mode.[22,31] Due to the interaction of the SiO_4 tetrahedra with the MO_8 dodecahedra in the unit cell, the SiO_4 tetrahedra cannot be considered a strictly independent unit.[87] As a result of these interactions, there has yet to be a reporting of a spectrum with all 17 of the Raman-active modes for zircon structure-type materials.[83] The peak vibrational positions for stetindite under ambient pressure are displayed in Table 1

Table 1. Location of the Internal Vibration Modes of SiO_4 Tetrahedron of Stetindite in cm^{-1} and Comparison with Those of Some Other Zircon Structure-Type Materials under Ambient Pressures[55,56,57,8283,85,87,88]

	$\nu_1(A_{1g})$	$\nu_2(A_{1g})$	$\nu_3(B_{2g})$	$\nu_4(B_{2g})$	Ref
$CeSiO_4$	902	417	920	594	This Study
$CeSiO_4$	903	431	919	592	Estevenon et al.[55]
$CeSiO_4$	902	431	919	592	Estevenon et al.[56]
$CeSiO_4$	902	416	918	593	Strzelecki et al.[59]
$ZrSiO_4$	974	439	1008	608	Dawson et al.[82]
$HfSiO_4$	984	448	1018	620	Hoskins et al.[85]
$ThSiO_4$	894	439	920	593	Syme et al.[87]
$ThSiO_4$	887	438	914	592	Clavier et al.[83]
$USiO_4$	904	428	930	N.O.	Geisler et al.[88]
$USiO_4$	906	424	919	591	Clavier et al.[83]
$USiO_4$	903	424	918	592	Strzelecki et al.[59]

alongside other zircon structure-type orthosilicates.[55,56,59,8283,85,87,88] The peak position and standard error from each deconvolution are listed in Table S6. The $I\bar{4}_2d$ space group, which the HPLS structure belongs to, has 30 theoretical active Raman vibrational modes ($\Gamma = 3A_1 + 5B_1 + 4B_2 + 9E_g$), based on the D_{2d} point group. The authors recommend the work by Mihailova et al. for a more in depth discussion on the mode analysis of this space group.[31] The $I4_1/a$ space group has 18 theoreticaly active Raman vibrational modes ($\Gamma = 3A_g + 5B_g + 5E_g$), based upon the C^6_{4h} point group.[89−91] Of these 18 active modes, nine ($\Gamma_{int} = 2A_g + 3B_g + 2E_g$) can be assigned to the internal vibrations of the SiO_4 tetrahedron, while the remaining nine ($\Gamma_{ext} = A_g + 2B_g + 3E_g$) can be assigned to the external vibrations within the unit cell.[8990] The vibrational modes labeled ν_1, ν_2, ν_3, and ν_4 correspond to the internal vibrations. The symmetric and antisymmetric stretching motions are represented by ν_1 (A_g) and ν_3 ($B_g + E_g$), respectively, and the symmetric and antisymmetric bending modes correspond to ν_2 ($A_g + B_g$) and ν_4 ($B_g + E_g$), respectively. The motion of the external modes can be further be classified into rotational ($A_g + B_g$) and translational ($2B_g + 2E_g$) modes.[8990] The peak position and standard error from

https://doi.org/10.1021/acs.jpcc.2c06657
J. Phys. Chem. C XXXX, XXX, XXX−XXX

each deconvolution are listed in Table S7. As with zircon structure-type materials, not all of the vibrational modes are present in the scheelite phase due to lattice interaction. Here we used the peak assignments of Smirnov et al., Gucsik et al., Stangarone et al., Knittle and Williams, Gucsik et al., Manoun et al., Bauer et al., and Kaur and Sinha in order to assign the peaks present in the scheelite-structured phase.[5−7,9,22,91−93] The Raman spectra collected during decompression below 11.4 GPa, along with the recovered $CeSiO_4$ from the laser heating experiment resemble that of scheelite ($CaWO_4$), stolzite ($PbWO_4$), powellite ($CaMoO_4$), wulfenite ($PbMoO_4$), and other tungstate and molybdate minerals and materials.[89,90,94−96]

4. DISCUSSION

4.1. Pressure−Volume Equations of State.

Figure 4 shows the pressure dependence of the unit cell volumes of the different $CeSiO_4$ phases from the experiments and the fits of the second-order Birch−Murnaghan EOS.[97] The equation describing the second-order Birch−Murnaghan EOS is the following:

$$P = \frac{3K_0}{2}\left[\left(\frac{V_0}{V}\right)^{7/3} - \left(\frac{V_0}{V}\right)^{5/3}\right] \quad (1)$$

in which V_0 is the zero-pressure unit cell volume, V is the cell volume at a given pressure (P), and K_0 is bulk modulus.[97] The fits were performed with the EosFit7 software.[98] The program offers the possibility to use the uncertainties of the data points to derive a weighting scheme for the fit. The errors associated with both the measured pressure by ruby luminescence[62] and the derived lattice parameters are from the Rietveld analyses. While other studies on zircon-structured orthosilicates, such as the work of Ehlers et al.,[99] have used higher-ordered Birch−Murnaghan EOS to fit their experimental data, it was not needed in our work. When transforming the $P-V$ data into Eulerain strain (f_E) and a normalized stress, also referred to as normalized pressure (F_E), the data plots reasonably well along a horizonal line (Figure S5).[100] This indicates that the data can be fitted to a second-order Birch−Murnaghan EOS with reasonable confidence.

The fits performed on the zircon-structured polymorph used the data collected from 0.2 ± 0.2 to 14.5 ± 0.7 GPa and applied the data collected from both sets of experiments (Figure 4). The resulting fit to the second-order Birch−Murnaghan EOS yielded a V_0 of 300.8(3) Å^3 and a K_0 of 171(5) GPa. The derived V_0 (300.8(3) Å^3) from the fitting was in good agreement with the previously reported unit cell volumes of the zircon-structured polymorph by Estevenon et al. (299.53(1) Å^3),[55] Estevenon et al. (299.85(2) Å^3),[56] and Strzelecki et al. (300.47(4) Å^3).[59] At higher pressures, we applied second-order Birch−Murnaghan EOS fitting on scheelite-structure polymorph, using the decompression data collected between 28.6 and 4.1 GPa from only the in situ high-pressure laser-heated experiments, from which we yielded a V_0 of 276(3) Å^3 and a K_0 of 221(40) GPa (Figure 4).

If the zircon structure was used between 15 and 19 GPa for Rietveld analysis, it resulted in a deviation to lower-than-expected volumes (Figure S6). This indicates that, at these pressures, $CeSiO_4$ structure is undergoing a considerable amount of softening. Such behavior is similar to what was found by Van Western et al. when synthetically pure zircon was compressed above 19.7 GPa.[101] Stangarone et al. argued that the deviation to smaller volumes observed by Van Westrenen et al. was a consequence of the displacive phase transition to the HPLS phase.[22] This is also the rational basis on which we assumed that $CeSiO_4$ might have undergone the HPLS phase transition in this pressure region and used the HPLS structure (space group: $I\bar{4}_2d$) to analyze the XRD data collected between 15 and 19 GPa (Figures 4 and S6). Applying a second-order Birch−Murnaghan EOS fitting yielded a V_0 of 309(1) Å^3 and a K_0 of 105(4) GPa for the HPLS $CeSiO_4$, reflecting a softer bulk modulus than the zircon-structure phase at lower pressures. This lattice softening may signify an intermediate nature of the HPLS phase between zircon and scheelite and sequentially trigger the transition to the latter. If one believes the argument of Stangarone et al. and fits the $P-V$ data of Van Westrenen et al.,[101] for zircon from 19.66 to 22.16 GPa to a second-order Birch−Murnaghan EOS, it yields a V_0 of 288(17) Å^3 and a K_0 of 72(30) GPa, which again show a softening of the bulk modulus for potentially a HPLS-structured material.

In order to further evaluate the validity of our derived K_0 and V_0, we employed two verification methods. The first method of verification is based on fitting unit cell parameters a and c to a one-dimensional form of the Birch−Murnaghan EOS (Figure 5). This was accomplished by replacing the V term with a^3 or c^3 and V_0 with a_0^3 or c_0^3 in eq 1 to yield values for a_0, M_a, c_0, and M_c. The variables, M_a and M_c are respectively the axial linear moduli of the a and c axes. The values derived for M_a and M_c were used to further check the previously derived K_0 and give confidence in these values through the following relation:

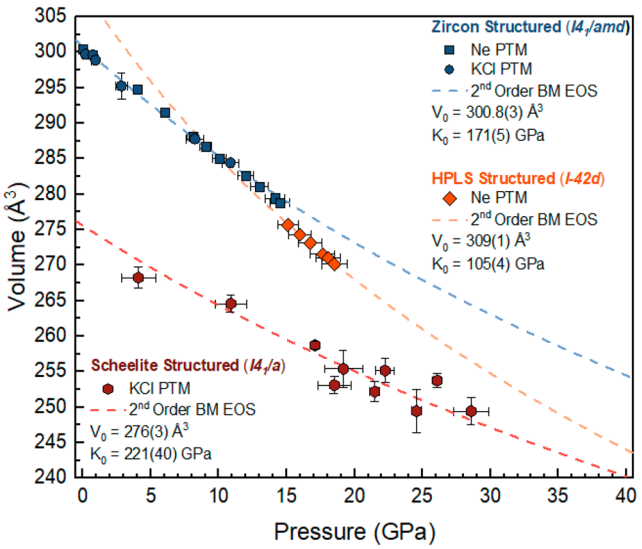

Figure 4. Unit cell volume of $CeSiO_4$ as a function of pressure. Blue symbols represent the low-pressure zircon-type ($I4_1/amd$) phase; orange symbols represent the intermediate-pressure HPLS-type ($I\bar{4}_2d$) phase; red symbols represent the high-pressure scheelite-type ($I4_1/a$) phase; squares represent the data collected at beamline 16-BM-D where Ne was used as the PTM; and circles represent the data collected at beamline 13-ID-D where KCl was used as the PTM. The dashed traces are the second-order Birch−Murnaghan EOS.[98] For the zircon-type structure, it was fitted from 0.2 to 14.5 GPa, using the data collected with both PTM. For the HPLS structure, it was fitted from 15.1 to 18.5 GPa, using the data collected with Ne as the PTM. For the scheelite-type structure, it was fitted from 4.1 to 28.6 GPa, using data only collected with KCl as the PTM.

https://doi.org/10.1021/acs.jpcc.2c06657
J. Phys. Chem. C XXXX, XXX, XXX−XXX

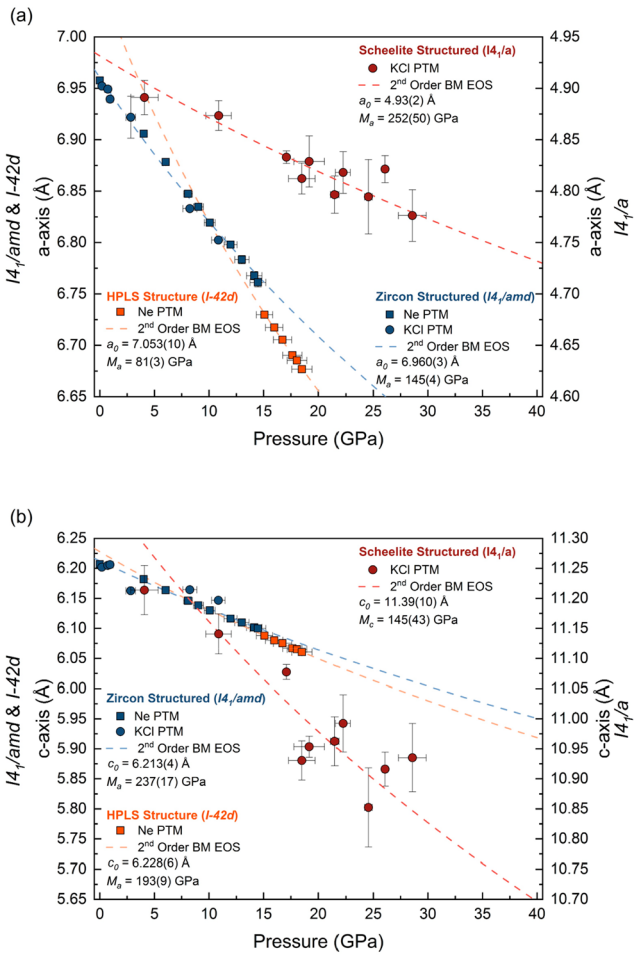

Figure 5. Unit cell parameters of $CeSiO_4$ as a function of pressure. (a) Variation in the *a*-axis and (b) variation in the *c*-axis for each of the phases. Blue symbols represent the low-pressure zircon-type ($I4_1/amd$) phase; orange symbols represent the intermediate-pressure HPLS-type ($I\bar{4}_2d$) phase; red symbols represent the high-pressure scheelite-type ($I4_1/a$) phase; squares represent the data collected at beamline 16-BM-D where Ne was used as the PTM; and circles represent the data collected at beamline 13-ID-D where KCl was used as the PTM. The dashed traces are the second-order Birch–Murnaghan EOS:[98] for zircon type, this was fit from 0.2 to 10.1 GPa, using the data collected with both PTM; for the HPLS, this was fit from 15.1 to 18.5 GPa, using the data collected with Ne as the PTM; and for the scheelite-type, it was fitted from 4.1 to 28.6 GPa, using data only collected with KCl as the PTM.

$$K_{0,lm} = 3\left(\frac{1}{M_a} + \frac{1}{M_a} + \frac{1}{M_c}\right)^{-1} \quad (2)$$

For stetindite, the one-dimensional form of the Birch–Murnaghan EOS yielded a_0 = 6.960(3) Å, M_a = 145(4) GPa, c_0 = 6.213(4) Å, and M_c = 237(17) GPa. Using the values of a_0 and c_0, $V_{0,lm}$ was calculated to be 300.8(3) Å^3, in good agreement with the unit cell volume V_0 of 301.0(3) Å^3 (Figure 4). $K_{0,lm}$ was calculated by taking the derived values of M_a and M_c into eq 2 to be 166(4) GPa, again in good agreement with K_0 of 171(5) GPa from the volumetric data. Applying the one-dimensional Birch–Murnaghan EOS to data of HPLS phase yielded the following values: a_0 = 7.053(10) Å, M_a = 81(3) GPa, c_0 = 6.228(6) Å, and M_c = 193(9) GPa. $V_{0,lm}$ of HPLS was calculated to be 309.8(9) Å^3, in agreement with V_0 of 309(1) Å^3. The derived $K_{0,lm}$ of HPLS, 101(3) GPa, also agreed within error with K_0 of 105(4) GPa. Lastly, the scheelite phase has the following values fitted from the one-dimensional Birch–Murnaghan EOS: a_0 = 4.93(2) Å, M_a = 252(50) GPa, c_0 = 11.39(10) Å, and M_c = 145(43) GPa. $V_{0,lm}$ of scheelite was evaluated to be 277(3) Å^3, which agreed with V_0 of 276(3) Å^3. The derived $K_{0,lm}$ of scheelite, 202(35) GPa, also agreed within error with K_0 of 221(40) GPa.

Through the first verification method, it was possible to gain anisotropic insight into how the three polymorphs respond to pressure. For the low-pressure zircon-structured polymorph, the linear modulus along the *c*-axis (M_c= 237(17) GPa) is 1.63 ± 0.13 times that along the *a*-axis (M_a = 145(4) GPa), suggesting more compressibility along the *a*-axis. The anisotropic behavior can be explained by the arrangement of TO_4 tetrahedra and MO_8 dodecahedra (Figure 1a,b). The MO_8 dodecahedra can be depicted as two intersected disphenoidal MO_4 forms: edge-sharing $MO1_4$ alternating with TO_4 along the *c*-axis, and $MO2_4$ corner-sharing with another $MO2_4$ tetrahedra forming a zigzagging chain along the *a*-axis (Figure 1a,b).[2,102,103] Higher freedom of corner-sharing $MO2_4$ tetrahedra makes the zircon structure more flexible along the *a*-axis during compression, while the edge-sharing rigid TO_4 arranging along the *c*-axis is less compressible.[103,104] Thus, due to the higher repulsion experienced due to the edge sharing over corner sharing, the *c*-axis contracts at a slower rate than that of the *a*-axis.

Because of the similarity in structure, the HPLS phase is also more compressible along the *a*-axis than the *c*-axis, with the degree of anisotropy further increased. This is evidenced by the linear moduli of HPLS along the *c*-axis (M_c = 193(9) GPa) is 2.38 times that along the *a*-axis (M_a = 81(3) GPa). Such an increase in anisotropic behavior can be explained by the rotation of the SiO_4 tetrahedra around the *c*-axis. Due to this symmetric operation with respect to the zircon structure, there is an addition SiO_4–MO_8–SiO_4 edge-sharing chain that is formed and the number of [001] channels increased from 2 to 4 per unit cell (Figure 1). As stated previously, for the zircon structure these chains cause the anisotropic compressibility behavior; therefore, an increase in the number of these moieties in the unit cell would be expected to promote anisotropy. Moreover, the increase in the degree of corner sharing along the *a*-axis (Figure 1c,d) is the reason for the dramatic decrease in the bulk moduli of the HPLS phase with respect to stetindite.

After the second phase transformation, the high-pressure scheelite-structured polymorph has an inverse anisotropic behavior that is more compressible along the *c*-axis than the *a*-axis, similar to the anisotropic behavior that was found for synthetic reidite (M_c/M_a = ~1.5).[105] This is shown by the linear modulus along the *a*-axis (M_a = 252(50) GPa) is 1.73 ± 0.61 times than that along the *c*-axis (M_c = 145(43) GPa). The anisotropic behavior arises from the arrangement of the MO_8 dodecahedra which form an edge-sharing chain that zigzags along the *a*-axis.[2,106] These chains are then cross-linked by the TO_4 tetrahedra corner sharing with the MO_8 dodecahedra parallel to the *c*-axis (Figure 1e,f).[2,106] Subsequently, it is the corner sharing parallel to the *c*-axis that gives rise to the anisotropic compression. While such anisotropic behavior is the inverse to what was found for both the zircon structured and HPLS polymorphs, the mechanism of the prevalence of

https://doi.org/10.1021/acs.jpcc.2c06657
J. Phys. Chem. C XXXX, XXX, XXX–XXX

edge-sharing moieties in a specific crystallographic direction being the root cause of anisotropy is the same.

The second verification method is based on the empirical inverse relationship between bulk modulus and unit cell volume of isostructural inorganic materials.[107,108] Considering that the bulk modulus of a given material is dictated by the bulk moduli of its constituent polyhedra and their arrangement,[109] then the inverse relationship for isostructural inorganic compounds (having the same polyhedra arrangement) is only dictated by the bulk moduli of polyhedra. Then, obviously, the bulk modulus of polyhedron is inversely correlated with the ionic radius of its metal center as a result of electrostatic interactions (i.e., repulsive forces).[107,109−111] This has been demonstrated at length for simple (i.e., MgO and Al_2O_3) and complex oxides (i.e., $MgAl_2O_4$).[107,110,111] This verification method could only be applied to the zircon and scheelite structure polymorphs as there is no other study on bulk moduli of comparable HPLS polymorphs. The derived values for zircon are in good agreement with the empirically derived trends of isostructural silicates (Figure 6).[4,8,9,23,25,112−114] Similarly for the high-pressure scheelite-structured phase, the derived K_0 value 221(40) GPa agrees with those of $USiO_4$ with its experimental values of 195(6) GPa and computational values (density functional theory, DFT) of 212(1) GPa reported by Bauer et al.[9] Because eight-coordinated U^{4+} (1.00 Å) and Ce^{4+} (0.97 Å) are much closer in terms of ionic radii than those of Hf^{4+} (0.83 Å) and Zr^{4+} (0.84 Å),[49] the solid state behavior of stetindite is expected to be closer to coffinite than hafnon or zircon.

4.2. Grüneisen Parameter. The Raman peak positions as a function of pressure for $CeSiO_4$ up to 18.2 GPa are displayed in Figures 7 and 8. Due to the relatively low intensities of the antisymmetric deformation (ν_4), it was not able to be discerned from the background (Figure 3) and thus is not

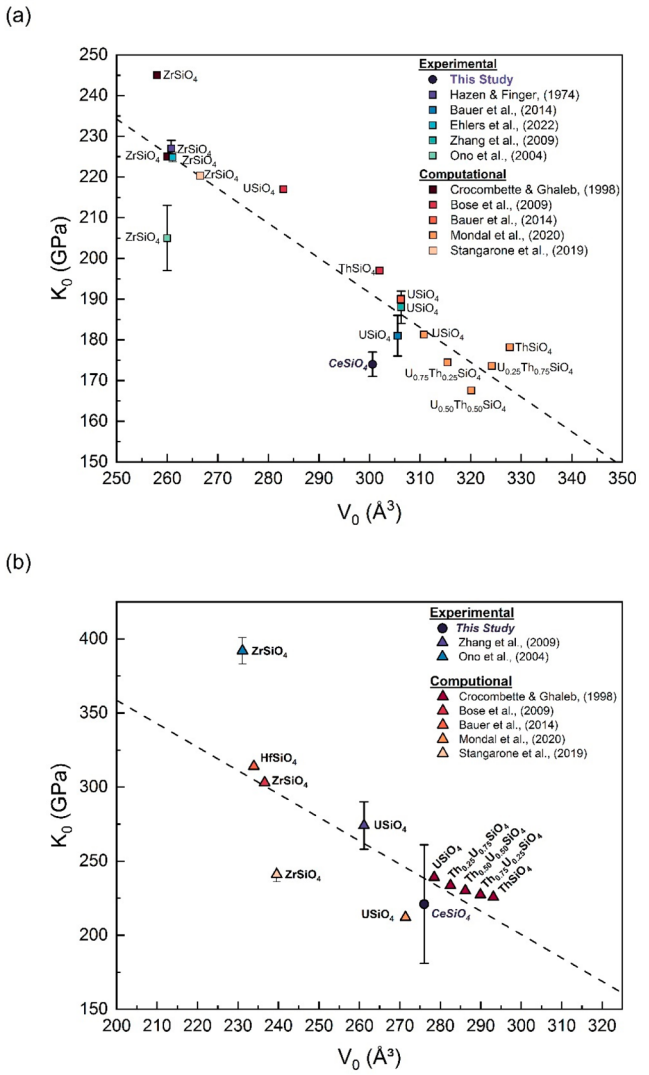

Figure 6. Comparison of bulk moduli of (a) zircon-type and (b) scheelite-type orthosilicate minerals.[4,8,9,23,25,112−114]

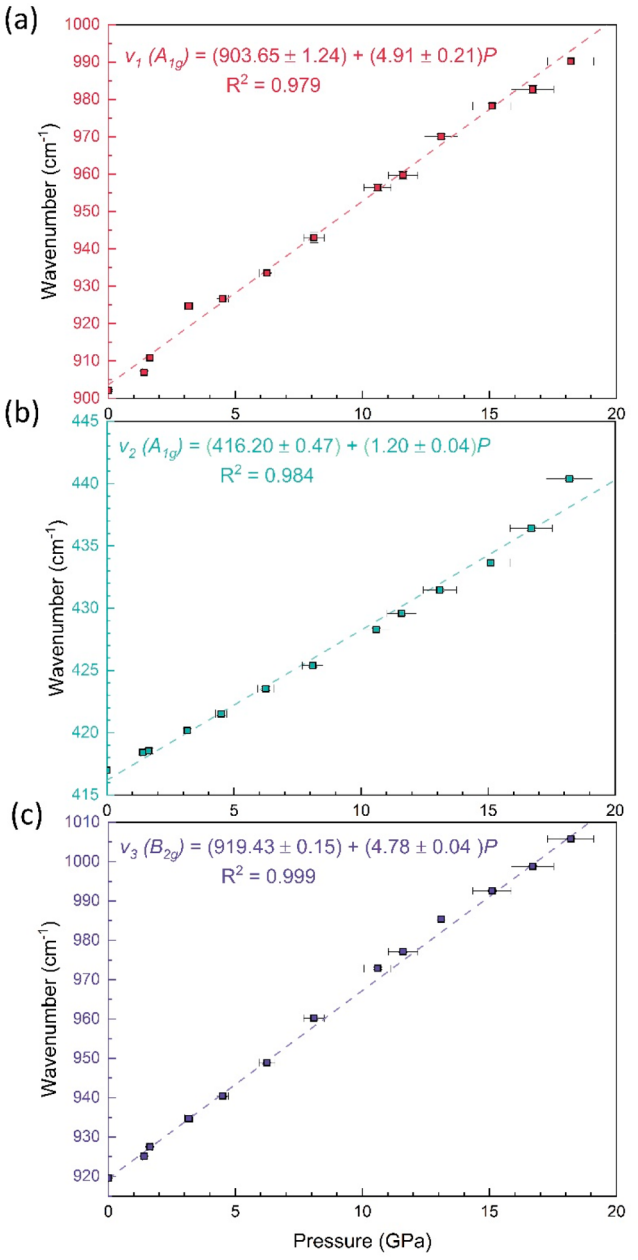

Figure 7. Pressure dependence of the internal Raman modes of stetindite from 0 to 18.2 GPa. (a) ν_1 (A_{1g}) SiO_4 symmetric stretching, (b) ν_2 (A_{1g}) SiO_4 symmetric bending, and (c) ν_3 (B_{2g}) SiO_4 antisymmetric stretching.

https://doi.org/10.1021/acs.jpcc.2c06657
J. Phys. Chem. C XXXX, XXX, XXX−XXX

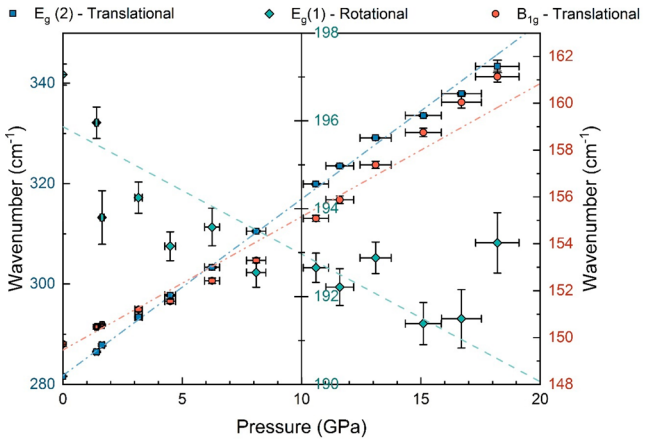

Figure 8. Pressure dependence of the external Raman modes of stetindite from 0 to 18.2 GPa.

included in Figure 7. The pressure derivatives of the peak positions ($d\nu/dP$) up to 18.2 GPa were computed by linear fits and are listed in Table 2. It is evident that all of the internal vibrational modes of the [SiO_4] tetrahedron show positive pressure dependence on the peak position (Figure 7). This positive pressure dependence of the peak position is consistent with decreasing the Si−O bond distances in the SiO_4 tetrahedron. This behavior contrast what was found in previous high-temperature Raman studies on $CeSiO_4$, where a negative pressure derivative of the internal vibrational modes due to an increasing of the Si−O bond distance of the SiO_4 tetrahedron was found.[59] Two of the external modes, E_g (2) and B_{1g}, were also found to have positive pressure derivatives (Figure 8). However, the E_g (1) external mode exhibits a negative pressure derivative until 15.1 GPa. The cause of this negative pressure derivative is a result of the twisting of the SiO_4 and CeO_8 polyhedra about the *c*-axis during the zircon to HPLS phase transformation.[28,31] The E_g (1) mode then begins to demonstrate some hardening above 15.1 GPa, as it begins to demonstrate a positive pressure derivative (Figure 8). The inflection point of the E_g (1) mode shifting from a negative pressure derivative to a positive pressure derivative indicates the transformation of the E_g (1) mode of the zircon structure to an E mode of the HPLS-structured phase.[31] This behavior of this lattice mode is consistent with that predicted by Stangarone et al. and observed by Mihailova et al. in the zircon → HPLS phase transformation.[22,31] Overall, for stetindite, the individual vibrational mode shifts ($d\nu/dP$) are comparable to those of other isostructural orthosilicate minerals (zircon, hafnon, and coffinite), which are listed in Table 2.[6,7,9]

Using the obtained K_0 value for stetindite (reported in the previous section), in conjunction with vibrational mode shifts, we have derived the mode Grüneisen parameters (γ_i). γ_i were derived through the following equation:

$$\gamma_i = \left(\frac{K_0}{\nu_0}\right)\left(\frac{d\nu}{dP}\right) \quad (3)$$

The derived values for the γ_i for stetindite are reported in Table 2. Both the value of vibrational mode shifts and the bulk modulus values are comparable to the other zircon-structure-type orthosilicates, so are the γ_i. When comparing to other nonzircon-type orthosilicate minerals, such as olivine ($(Mg, Fe)_2SiO_4$),[115−117] garnet ($(Mg, Ca, Fe)_3Al_2Si_3O_{12}$)[118,119] and aluminum silicate (Al_2SiO_5),[120], we found that the obtained pressure derivatives for the stretching and deformation modes of the silica tetrahedra are comparable. Yet, they deviate from these of γ_i. The reason for such a deviation in the γ_i between the different orthosilicates is because the zircon-structure-type are significantly less compressible, possessing higher K_0 values than those of olivine and garnet, thus resulting in higher γ_i values.

A similar procedure was applied to the high-pressure scheelite-structure phase. The pressure derivatives of the peak positions ($d\nu/dP$) collected during the decompression from 11.4 GPa to ambient were computed by linear fits. They are listed in Table S8. It was found that all of the observable vibrational modes show positive pressure derivatives. Using the obtained K_0 value for the scheelite-structure phase, reported in the previous section, in conjunction with available vibrational mode shifts, we have derived the available γ_i using eq 3. These γ_i are tabulated in Table S8.

5. CONCLUSIONS

In this work, we present the first high-pressure study on synthetic stetindite by a combination of in situ high-pressure synchrotron powder X-ray diffraction up 36.0 ± 1.8 GPa, in situ high-pressure laser-heated synchrotron powder X-ray diffraction up 28.6 ± 1.3 GPa and temperature more than 3000 K, and in situ high-pressure Raman spectroscopy up to 43.0 ± 2.2 GPa. High pressure in these experiments was achieved by diamond anvil cells (DACs), with a variety of different pressure transmitting media. The transition of zircon to the HPLS phase was observed to occur at 15.1 GPa, evidenced by the softening of elastic moduli. It should be

Table 2. Pressure Derivatives ($d\nu/dP$) of the Vibrational Modes and Grüneisen Parameters (γ_i) of $CeSiO_4$ below 18.2 GPa and Comparison with the Values of Some Other Isostructural Minerals

	$d\nu_1/dP$ (cm^{-1}/GPa)	$d\nu_2/dP$ (cm^{-1}/GPa)	$d\nu_3/dP$ (cm^{-1}/GPa)	$d\nu_4/dP$ (cm^{-1}/GPa)	Method	Ref
$CeSiO_4$	4.9	1.2	4.8	N/A	Experimental	This Study
$HfSiO_4$	4.1	1.1	4.6	N/A	Experimental	Manoun et al.[7]
$ZrSiO_4$	4.1	1.1	4.8	N/A	Experimental	Knittle and Williams[6]
$USiO_4$	5.2	1.4	6.0	3.2	Experimental	Bauer et al.[9]
$USiO_4$	5.6	1.2	5.4	1.8	DFT	Bauer et al.[9]

	γ_1	γ_2	γ_3	γ_4	Method	Ref
$CeSiO_4$	0.95	0.50	0.90	N/A	Experimental	This Study
$ZrSiO_4$	1.0	0.57	1.1	N/A	Experimental	Knittle and Williams[6]
$USiO_4$	1.03	0.61	1.18	0.99	Experimental	Bauer et al.[9]
$USiO_4$	1.12	0.54	1.07	0.57	DFT	Bauer et al.[9]

https://doi.org/10.1021/acs.jpcc.2c06657
J. Phys. Chem. C XXXX, XXX, XXX−XXX

noted that the X-ray diffraction patterns of stetindite and HPLS phase were nearly identical, due to only a minuscule change in the symmetry between the $I4_1/amd$ and $I\bar{4}_2d$ space groups. Besides the evidence from the softening in bulk moduli, the emergence of the HPLS phase is supported by the change in the pressure derivative of the E_g (1) mode from negative to positive at 15.1 GPa, indicating its shifting from the E_g (1) mode of the zircon structure to an E mode of the HPLS structure. The phase transition of HPLS to scheelite occurred above 18.1 GPa. Scheelite is fully quenchable by means of synchrotron powder X-ray diffraction and Raman spectroscopy. The bulk moduli of stetindite, the HPLS, and the scheelite structure phases were determined by fitting to a second-ordered Birch–Murnaghan EOS to be 171(5), 105(4), and 221(40) GPa, respectively. The pressure derivatives of the vibrational modes of stetindite were consistent with those previously reported for other orthosilicate minerals, including pyrope ($Mg_3Al_2(SiO_4)_3$), forsterite (Mg_2SiO_4), zircon, hafnon, and coffinite. The reported γ_i are in good agreement with those reported for zircon, hafnon, and coffinite.

■ ASSOCIATED CONTENT

Supporting Information

The Supporting Information is available free of charge at https://pubs.acs.org/doi/10.1021/acs.jpcc.2c06657.

PXRD, refined lattice parameters, in situ high-P Raman, and equations of state (PDF)

■ AUTHOR INFORMATION

Corresponding Author

Xiaofeng Guo − *Department of Chemistry, Washington State University, Pullman, Washington 99164, United States; Alexandra Navrotsky Institute for Experimental Thermodynamics and Materials Science and Engineering Program, Washington State University, Pullman, Washington 99164, United States;* orcid.org/0000-0003-3129-493X; Email: x.guo@wsu.edu

Authors

Andrew Strzelecki − *Department of Chemistry, Washington State University, Pullman, Washington 99164, United States; Alexandra Navrotsky Institute for Experimental Thermodynamics and Materials Science and Engineering Program, Washington State University, Pullman, Washington 99164, United States; Earth and Environmental Sciences Division, Los Alamos National Laboratory, Los Alamos, New Mexico 87545, United States*

Xiaodong Zhao − *Department of Chemistry, Washington State University, Pullman, Washington 99164, United States; Alexandra Navrotsky Institute for Experimental Thermodynamics, Washington State University, Pullman, Washington 99164, United States*

Jason Baker − *Earth and Environmental Sciences Division, Los Alamos National Laboratory, Los Alamos, New Mexico 87545, United States*

Paul Estevenon − *ICSM, University of Montpellier, CNRS, CEA, ENSCM, Bagnols sur Cèze 30207, France; CEA, DES, ISEC, DMRC, University of Montpellier, Bagnols sur Cèze 30207, France*

Thomas Barral − *ICSM, University of Montpellier, CNRS, CEA, ENSCM, Bagnols sur Cèze 30207, France*

Adel Mesbah − *ICSM, University of Montpellier, CNRS, CEA, ENSCM, Bagnols sur Cèze 30207, France;* orcid.org/0000-0002-6905-2402

Dmitry Popov − *Advanced Photon Source, Argonne National Laboratory, Argonne, Illinois 60439, United States*

Stella Chariton − *Center for Advanced Radiation Sources, University of Chicago, Chicago, Illinois 60439, United States;* orcid.org/0000-0001-5522-0498

Vitali Prakapenka − *Center for Advanced Radiation Sources, University of Chicago, Chicago, Illinois 60439, United States*

Sohan Ahmed − *Department of Chemistry, Washington State University, Pullman, Washington 99164, United States*

Choong-Shik Yoo − *Department of Chemistry, Washington State University, Pullman, Washington 99164, United States; Materials Science and Engineering Program, Washington State University, Pullman, Washington 99164, United States;* orcid.org/0000-0002-2664-0730

Nicolas Dacheux − *ICSM, University of Montpellier, CNRS, CEA, ENSCM, Bagnols sur Cèze 30207, France;* orcid.org/0000-0003-1636-1313

Hongwu Xu − *Earth and Environmental Sciences Division, Los Alamos National Laboratory, Los Alamos, New Mexico 87545, United States; School of Molecular Sciences, and Center for Materials of the Universe, Arizona State University, Tempe Arizona 85287, United States*

Complete contact information is available at: https://pubs.acs.org/10.1021/acs.jpcc.2c06657

Notes

The authors declare no competing financial interest.

■ ACKNOWLEDGMENTS

This work was supported by the institutional funds from the Department of Chemistry at Washington State University (WSU) in the early stage, and later supported by the National Science Foundation (NSF), Division of Materials Research, under Award No. 2144792, and Division of Earth Sciences, under Award No. 2149848. A.S. also acknowledges the supported by the G. T. Seaborg Institute through a Summer Research Fellowship. C.-S.Y. at WSU also acknowledges the support by the NSF (DMR 2112653) and DOE-NNSA (DE-NA0003918). A portion of the research presented in this article was supported by the Laboratory Directed Research and Development (LDRD) program of Los Alamos National Laboratory (LANL) under Project No. 20180007 DR. LANL, an affirmative action/equal opportunity employer, is managed by Triad National Security, LLC, for the National Nuclear Security Administration of the U.S. Department of Energy under Contract 89233218CNA000001. A portion of this work was performed at HPCAT (Sector 16), Advanced Photon Source (APS), Argonne National Laboratory. HPCAT operations are supported by DOE-NNSA's Office of Experimental Sciences. A portion of this work was performed at GeoSoilEnviroCARS (The University of Chicago, Sector 13), Advanced Photon Source (APS), Argonne National Laboratory. GeoSoilEnviroCARS is supported by the NSF—Earth Sciences (EAR−1634415). This research used resources of the Advanced Photon Source, a U.S. Department of Energy (DOE) Office of Science User Facility operated for the DOE Office of Science by Argonne National Laboratory under Contract No. DE-AC02-06CH11357.

https://doi.org/10.1021/acs.jpcc.2c06657
J. Phys. Chem. C XXXX, XXX, XXX−XXX

REFERENCES

(1) Speer, J. A. Zircon. *Rev. Mineral. Geochem.* **1980**, *5*, 67−112.
(2) Finch, R. J.; Hanchar, J. M.; Zircon; Hanchar, J. M.; Hoskin, P. W. O. Structure and Chemistry of Zircon and Zircon-Group Minerals. *Rev. Mineral. Geochem.* **2003**, *53*, 1−26.
(3) Reid, A. F.; Ringwood, A. E. Newly Observed High Pressure Transformation in Mn_3O_4, $CaAl_2O4$, and $ZrSiO_4$. *Earth Planet. Sci. Lett.* **1969**, *6*, 205−208.
(4) Hazen, R. M.; Finger, L. M. Crystal Structure and Compressibility of Zircon at High Pressure. *Am. Mineral.* **1979**, *64*, 196−201.
(5) Gucsik, A.; Zhang, M.; Koeberl, C.; Salje, E. K. H.; Redfern, S. A. T.; Pruneda, J. M. Infrared and Raman Spectra of $ZrSiO_4$ Experimentally Shocked at High Pressures. *Mineral. Mag.* **2004**, *68* (5), 801−811.
(6) Knittle, E.; Williams, Q. High-Pressure Raman Spectroscopy of $ZrSiO_4$: Observation of the Zircon to Scheelite Transition at 300 K. *Am. Mineral.* **1993**, *78* (3−4), 245−252.
(7) Manoun, B.; Downs, R. T.; Saxena, S. K. A High-Pressure Raman Spectroscopic Study of Hafnon, $HfSiO_4$. *Am. Mineral.* **2006**, *91* (11−12), 1888−1892.
(8) Zhang, F. X.; Pointeau, V.; Shuller, L. C.; Reaman, D. M.; Lang, M.; Liu, Z.; Hu, J.; Panero, W. R.; Becker, U.; Poinssot, C.; Ewing, R. C. Structural Transitions and Electron Transfer in Coffinite, $USiO_4$, at High Pressure. *Am. Mineral.* **2009**, *94* (7), 916−920.
(9) Bauer, J. D.; Labs, S.; Weiss, S.; Bayarjargal, L.; Morgenroth, W.; Milman, V.; Perlov, A.; Curtius, H.; Bosbach, D.; Zänker, H.; Winkler, B. High-Pressure Phase Transition of Coffinite, $USiO_4$. *J. Phys. Chem. C* **2014**, *118* (43), 25141−25149.
(10) Zhang, F. X.; Lang, M.; Ewing, R. C.; Lian, J.; Wang, Z. W.; Hu, J.; Boatner, L. A. Pressure-Induced Zircon-Type to Scheelite-Type Phase Transitions in $YbPO_4$ and $LuPO_4$. *J. Solid State Chem.* **2008**, *181* (10), 2633−2638.
(11) Lacomba-Perales, R.; Errandonea, D.; Meng, Y.; Bettinelli, M. High-Pressure Stability and Compressibility of APO_4 (A = La, Nd, Eu, Gd, Er, and Y) Orthophosphates: An x-Ray Diffraction Study Using Synchrotron Radiation. *Phys. Rev. B - Condens. Matter Mater. Phys.* **2010**, *81* (6), 1−9.
(12) López-Solano, J.; Rodríguez-Hernández, P.; Muñoz, A.; Gomis, O.; Santamaría-Perez, D.; Errandonea, D.; Manjón, F. J.; Kumar, R. S.; Stavrou, E.; Raptis, C. Theoretical and Experimental Study of the Structural Stability of $TbPO_4$ at High Pressures. *Phys. Rev. B - Condens. Matter Mater. Phys.* **2010**, *81* (14), 1−9.
(13) Gomis, O.; Lavina, B.; Rodríguez-Hernández, P.; Muñoz, A.; Errandonea, R.; Errandonea, D.; Bettinelli, M. High-Pressure Structural, Elastic, and Thermodynamic Properties of Zircon-Type $HoPO_4$ and $TmPO_4$. *J. Phys.: Condens. Matter* **2017**, *29* (9), 095401.
(14) Heuser, J. M.; Palomares, R. I.; Bauer, J. D.; Rodriguez, M. J. L.; Cooper, J.; Lang, M.; Scheinost, A. C.; Schlenz, H.; Winkler, B.; Bosbach, D.; et al. Structural Characterization of (Sm, Tb) PO_4 Solid Solutions and Pressure-Induced Phase Transitions. *J. Eur. Ceram. Soc.* **2018**, *38* (11), 4070−4081.
(15) Wang, X.; Loa, I.; Syassen, K.; Hanfland, M.; Ferrand, B. Structural Properties of the Zircon- and Scheelite-Type Phases of YVO_4 at High Pressure. *Phys. Rev. B* **2004**, *70* (6), 064109.
(16) Errandonea, D.; Kumar, R. S.; Achary, S. N.; Tyagi, A. K. In Situ High-Pressure Synchrotron x-Ray Diffraction Study of $CeVO_4$ and $TbVO_4$ up to 50 GPa. *Phys. Rev. B - Condens. Matter Mater. Phys.* **2011**, *84* (22), 1−8.
(17) Huang, Z.; Zhang, L.; Pan, W. Synthesis, Lattice Dynamics, and Mechanical Properties of a High-Pressure Scheelite Phase of RVO_4. *Inorg. Chem.* **2012**, *51* (21), 11235−11237.
(18) Errandonea, D.; Popescu, C.; Achary, S. N.; Tyagi, A. K.; Bettinelli, M. In Situ High-Pressure Synchrotron X-Ray Diffraction Study of the Structural Stability in $NdVO_4$ and $LaVO_4$. *Mater. Res. Bull.* **2014**, *50*, 279−284.
(19) Panchal, V.; Errandonea, D.; Manjón, F. J.; Muñoz, A.; Rodríguez-Hernández, P.; Bettinelli, M.; Achary, S. N.; Tyagi, A. K. High Pressure Phase Transitions in $NdVO_4$. *AIP Conf. Proc.* **2015**, *1665*, 030006.
(20) Garg, A. B.; Errandonea, D. High-Pressure Powder x-Ray Diffraction Study of $EuVO_4$. *J. Solid State Chem.* **2015**, *226*, 147−153.
(21) Ruiz-Fuertes, J.; Martínez-García, D.; Marqueño, T.; Errandonea, D.; Macleod, S. G.; Bernert, T.; Haussühl, E.; Santamaría-Pérez, D.; Ibáñez, J.; Mallavarapu, A.; et al. High-Pressure High-Temperature Stability and Thermal Equation of State of Zircon-Type Erbium Vanadate. *Inorg. Chem.* **2018**, *57* (21), 14005−14012.
(22) Stangarone, C.; Angel, R. J.; Prencipe, M.; Mihailova, B.; Alvaro, M. New Insights into the Zircon-Reidite Phase Transition. *Am. Mineral.* **2019**, *104* (6), 830−837.
(23) Luo, W.; Ahuja, R. High Pressure Structural Phase Transition in Zircon ($ZrSiO_4$). *J. Phys. Conf. Ser.* **2008**, *121*, 0220014.
(24) Bose, P. P.; Mittal, R.; Chaplot, S. L. Lattice Dynamics and High Pressure Phase Stability of Zircon Structured Natural Silicates. *Phys. Rev. B - Condens. Matter Mater. Phys.* **2009**, *79* (17), 1−8.
(25) Tange, Y.; Takahashi, E. Stability of the High-Pressure Polymorph of Zircon ($ZrSiO_4$) in the Deep Mantle. *Phys. Earth Planet. Inter.* **2004**, *143* (1−2), 223−229.
(26) Ono, S.; Tange, Y.; Katayama, I.; Kikegawa, T. Equation of State of $ZrSiO_4$ Phases in the Upper Mantle. *Am. Mineral.* **2004**, *89*, 185−188.
(27) Ono, S.; Funakoshi, K.; Nakajima, Y.; Tange, Y.; Katsura, T. Phase Transition of Zircon at High P-T Conditions. *Contrib. to Mineral. Petrol.* **2004**, *147* (4), 505−509.
(28) Farnan, I.; Balan, E.; Pickard, C. J.; Mauri, F. The Effects of Radiation on Local Structure in the Crystalline Fraction of $ZrSiO_4$: Investigating the 29Si NMR Response to Pressure in Zircon and Reidite. *Am. Mineral.* **2003**, *88*, 1663−1667.
(29) Glass, B. P.; Liu, S.; Leavens, P. B. Reidite: An Impact-Produced High-Pressure Polymorph of Zircon Found in Marine Sediments. *Am. Mineral.* **2002**, *87* (4), 562−565.
(30) Du, J.; Devanathan, R.; RenéCorrales, L.; Weber, W. J. First-Principles Calculations of the Electronic Structure, Phase Transition and Properties of $ZrSiO_4$ Polymorphs. *Comput. Theor. Chem.* **2012**, *987*, 62−70.
(31) Mihailova, B.; Waeselmann, N.; Stangarone, C.; Angel, R. J.; Prencipe, M.; Alvaro, M. The Pressure-Induced Phase Transition(s) of $ZrSiO_4$: Revised: Experimental Proof for the Existence of a New High-Pressure Polymorph of Zircon. *Phys. Chem. Miner.* **2019**, *46* (8), 807−814.
(32) Ewing, R. C.; Wang, L. M. Phosphates as Nuclear Waste Forms. In *Phosphates: Geochemical, Geobiological and Materials Importance*; Kohn, M. J., Rakovan, J., Hughes, J. M., Eds.; Mineralogical Society of America, 2002; Vol. *48*, pp 673−700. DOI: 10.2138/rmg.2002.48.18.
(33) Boatner, L. A. Synthesis, Structure, and Properties of Monazite, Pretulite, and Xenotime. *Reviews in Mineralogy and Geochemistry* **2002**, *48*, 87−121.
(34) Orlova, A. I.; Ojovan, M. I. Ceramic Mineral Waste-Forms for Nuclear Waste Immobilization. *Materials (Basel).* **2019**, *12* (16), 2638.
(35) Rafiuddin, M. R.; Grosvenor, A. P. Probing the Effect of Radiation Damage on the Structure of Rare-Earth Phosphates. *J. Alloys Compd.* **2015**, *653*, 279−289.
(36) Boatner, L. A.; Abraham, M. M.; Sales, B. C. Lanthanide Orthophosphate Ceramics for the Disposal of Actinide-Contaminated Nuclear Wastes. *Inorg. Chim. Acta* **1984**, *94* (1−3), 146−148.
(37) Lumpkin, G. R. Ceramic Waste Forms for Actinides. *Elements* **2006**, *2* (6), 365−372.
(38) Ewing, R. C.; Lutze, W.; Weber, W. J. Zircon: A Host-Phase for the Disposal of Weapons Plutonium. *J. Mater. Res.* **1995**, *10* (2), 243−246.
(39) Guo, X.; Navrotsky, A.; Kukkadapu, R. K.; Engelhard, M. H.; Lanzirotti, A.; Newville, M.; Ilton, E. S.; Sutton, S. R.; Xu, H. Structure and Thermodynamics of Uranium-Containing Iron Garnets. *Geochim. Cosmochim. Acta* **2016**, *189*, 269−281.
(40) Guo, X.; Szenknect, S.; Mesbah, A.; Clavier, N.; Poinssot, C.; Wu, D.; Xu, H.; Dacheux, N.; Ewing, R. C.; Navrotsky, A. Energetics

https://doi.org/10.1021/acs.jpcc.2c06657
J. Phys. Chem. C XXXX, XXX, XXX−XXX

of a Uranothorite ($Th_{1-X}U_xSiO_4$) Solid Solution. *Chem. Mater.* **2016**, *28* (19), 7117−7124.
(41) Guo, X.; Tavakoli, A. H.; Sutton, S.; Kukkadapu, R. K.; Qi, L.; Lanzirotti, A.; Newville, M.; Asta, M.; Navrotsky, A. Cerium Substitution in Yttrium Iron Garnet: Valence State, Structure, and Energetics. *Chem. Mater.* **2014**, *26* (2), 1133−1143.
(42) Chung, C. K.; O'Quinn, E. C.; Neuefeind, J. C.; Fuentes, A. F.; Xu, H.; Lang, M.; Navrotsky, A. Thermodynamic and Structural Evolution of Mechanically Milled and Swift Heavy Ion Irradiated $Er_2Ti_2O_7$ Pyrochlore. *Acta Mater.* **2019**, *181*, 309−317.
(43) Helean, K. B.; Navrotsky, A.; Vance, E. R.; Carter, M. L.; Ebbinghaus, B.; Krikorian, O.; Lian, J.; Wang, L. M.; Catalano, J. G. Enthalpies of Formation of Ce-Pyrochlore, $Ca_{0.93}Ce_{1.00}Ti_{2.035}O_{7.00}$, U-Pyrochlore, $Ca_{1.46}U^{4+}_{0.23}U^{6+}_{0.46}Ti_{1.85}O_{7.00}$ and Gd-Pyrochlore, $Gd_2Ti_2O_7$: Three Materials Relevant to the Proposed Waste Form for Excess Weapons Plutonium. *J. Nucl. Mater.* **2002**, *303* (2−3), 226−239.
(44) Neumeier, S.; Kegler, P.; Arinicheva, Y.; Shelyug, A.; Kowalski, P. M.; Schreinemachers, C.; Navrotsky, A.; Bosbach, D. Thermochemistry of $La_{1-x}Ln_xPO_4$-Monazites (Ln = Gd, Eu). *J. Chem. Thermodyn.* **2017**, *105*, 396−403.
(45) Ewing, R. C. Nuclear Waste Forms for Actinides. *Proc. Natl. Acad. Sci. U. S. A.* **1999**, *96* (7), 3432−3439.
(46) Ushakov, S. V.; Gong, W.; Yagokina, M. M.; Helean, K. B.; Lutze, W.; Ewing, R. C. Solid Solutions of Ce, U, and Th in Zircon. *Ceram. Trans.* **1999**, *93*, 357−363.
(47) Keller, V. C. Untersuchungen Über Die Germanate Und Silikate Des Typs ABO_4 Der Vierwertigen Elemente Thorium Bis Americium. *Nukleonik* **1963**, *5*, 41−48.
(48) Estevenon, P.; Welcomme, E.; Tamain, C.; Jouan, G.; Szenknect, S.; Mesbah, A.; Poinssot, C.; Moisy, P.; Dacheux, N. Formation of $PuSiO_4$ under Hydrothermal Conditions. *Dalt. Trans.* **2020**, *49*, 6434.
(49) Shannon, R. D. Revised Effective Ionic Radii and Systematic Studies of Interatomic Distances in Halides and Chalcogenides. *Acta Crystallogr., Sect. A* **1976**, *32* (5), 751−767.
(50) Zamoryanskaya, M. V.; Burakov, B. E. Feasibility Limits in Using Cerium as a Surrogate for Plutonium Incorporation in Zircon, Zirconia and Pyrochlore. *Mater. Res. Soc. Symp. - Proc.* **2000**, *663*, 301−306.
(51) Putnam, R. L.; Navrotsky, A.; Cordfunke, E. H. P.; Huntelaar, M. E. Thermodynamics of Formation of Two Cerium Aluminum Oxides, $CeAlO_{3(s)}$ and $CeAl_{12}O_{19.918(s)}$, and Cerium Sesquioxide, $Ce_2O_{3(s)}$ At T= 298.15 K. *J. Chem. Thermodyn.* **2000**, *32* (7), 911−921.
(52) Putnam, R. L.; Gallegos, U. F.; Ebbinghaus, B. B.; Navrotsky, A.; Helean, K. B.; Ushakov, S. V.; Woodfield, B. F.; Boerio-Goates, J.; Williamson, M. A. *Formation Energetics of Ceramic Phases Related to Surplus Plutonium Disposition*, Report No. LA-UR-00-1960; Los Alamos National Laboratory, 2000.
(53) Marra, J. C.; Cozzi, A. D.; Pierce, R. A.; Pareizs, J. M.; Jurgensen, A. R.; Missimer, D. M. Cerium as a Surrogate in the Plutonium Immobilized Form. In *Environmental Issues and Waste Management Technologies in the Ceramic and Nuclear Industries*; Smith, G. L., Sundaram, S. K., Spearing, D. R., Eds.; American Ceramic Society, 2002; pp 381−388. DOI: 10.1002/9781118371435.ch36.
(54) Schlüter, J.; Malcherek, T.; Husdal, T. A. The New Mineral Stetindite, $CeSiO_4$, a Cerium End-Member of the Zircon Group. *Neues Jahrb. fur Mineral. Abhandlungen* **2009**, *186* (2), 195−200.
(55) Estevenon, P.; Welcomme, E.; Szenknect, S.; Mesbah, A.; Moisy, P.; Poinssot, C.; Dacheux, N. Preparation of $CeSiO_4$ from Aqueous Precursors under Soft Hydrothermal Conditions. *Dalt. Trans.* **2019**, *48* (22), 7551−7559.
(56) Estevenon, P.; Kaczmarek, T.; Vadot, F.; Dumas, T.; Solari, P. L.; Welcomme, E.; Szenknect, S.; Mesbah, A.; Moisy, P.; Poinssot, C.; Dacheux, N. Formation of $CeSiO_4$ from Cerium (III) Silicate Precursors. *Dalt. Trans.* **2019**, *48*, 10455−10463.
(57) Strzelecki, A. C.; Bourgeois, C.; Kriegsman, K. W.; Estevenon, P.; Wei, N.; Szenknect, S.; Mesbah, A.; Wu, D.; Ewing, R. C.; Dacheux, N.; Guo, X. Thermodynamics of $CeSiO_4$: Implications for Actinide Orthosilicates. *Inorg. Chem.* **2020**, *59* (18), 13174−13183.
(58) Strzelecki, A. C.; Kriegsman, K. W.; Estevenon, P.; Goncharov, V.; Bai, J.; Szenknect, S.; Mesbah, A.; Wu, D.; McCloy, J. S.; Dacheux, N.; Guo, X. High-Temperature Thermodynamics of Cerium Silicates, A-$Ce_2Si_2O_7$ and $Ce_{4.67}(SiO_4)_3O$. *ACS Earth Space Chem.* **2020**, *4* (11), 2129−2143.
(59) Strzelecki, A. C.; Barral, T.; Estevenon, P.; Mesbah, A.; Goncharov, V.; Baker, J.; Bai, J.; Clavier, N.; Szenknect, S.; Migdissov, A.; et al. The Role of Water and Hydroxyl Groups in the Structures of Stetindite and Coffinite, $MSiO_4$ (M = Ce, U). *Inorg. Chem.* **2021**, *60*, 718−735.
(60) Hrubiak, R.; Sinogeikin, S.; Rod, E.; Shen, G. The Laser Micro-Machining System for Diamond Anvil Cell Experiments and General Precision Machining Applications at the High Pressure Collaborative Access Team. *Rev. Sci. Instrum.* **2015**, *86* (7), 072202.
(61) Park, C.; Popov, D.; Ikuta, D.; Lin, C.; Kenney-Benson, C.; Rod, E.; Bommannavar, A.; Shen, G. New Developments in Micro-X-Ray Diffraction and X-Ray Absorption Spectroscopy for High-Pressure Research at 16-BM-D at the Advanced Photon Source. *Rev. Sci. Instrum.* **2015**, *86* (7), 072205.
(62) Mao, H. K.; Xu, J.; Bell, P. M. Calibration of the Ruby Pressure Gauge to 800 Kbar under Quasi-Hydrostatic Conditions. *J. Geophys. Res.* **1986**, *91*, 4673−4676.
(63) Rivers, M.; Prakapenka, V. B.; Kubo, A.; Pullins, C.; Holl, C. M.; Jacobsen, S. D. The COMPRES/GSECARS Gas-Loading System for Diamond Anvil Cells at the Advanced Photon Source. *High Press. Res.* **2008**, *28* (3), 273−292.
(64) Prescher, C.; Prakapenka, V. B. DIOPTAS: A Program for Reduction of Two-Dimensional X-Ray Diffraction Data and Data Exploration. *High Press. Res.* **2015**, *35* (3), 223−230.
(65) Toby, B. H.; Von Dreele, R. B. GSAS-II: The Genesis of a Modern Open-Source All Purpose Crystallography Software Package. *J. Appl. Crystallogr.* **2013**, *46* (2), 544−549.
(66) Chidester, B. A.; Thompson, E. C.; Fischer, R. A.; Heinz, D. L.; Prakapenka, V. B.; Meng, Y.; Campbell, A. J. Experimental Thermal Equation of State of B2-KCl. *Phys. Rev. B* **2021**, *104* (9), 5−10.
(67) Lin, J. F.; Struzhkin, V. V.; Jacobsen, S. D.; Shen, G.; Prakapenka, V. B.; Mao, H. K.; Hemley, R. J. X-Ray Emission Spectroscopy with a Laser-Heated Diamond Anvil Cell: A New Experimental Probe of the Spin State of Iron in the Earth's Interior. *J. Synchrotron Radiat.* **2005**, *12* (5), 637−641.
(68) Shen, G.; Wang, Y.; Prakapenka, V.; Benmore, C. J.; Alp, E. E.; Ding, Y.; Yang, W. High-Pressure Research at the Advanced Photon Source. *Synchrotron Radiat. News* **2010**, *23* (3), 32−38.
(69) Prakapenka, V. B.; Kubo, A.; Kuznetsov, A.; Laskin, A.; Shkurikhin, O.; Dera, P.; Rivers, M. L.; Sutton, S. R. Advanced Flat Top Laser Heating System for High Pressure Research at GSECARS: Application to the Melting Behavior of Germanium. *High Press. Res.* **2008**, *28* (3), 225−235.
(70) Dewaele, A.; Belonoshko, A. B.; Garbarino, G.; Occelli, F.; Bouvier, P.; Hanfland, M.; Mezouar, M. High-Pressure-High-Temperature Equation of State of KCl and KBr. *Phys. Rev. B - Condens. Matter Mater. Phys.* **2012**, *85* (21), 1−7.
(71) Zha, C. S.; Mibe, K.; Bassett, W. A.; Tschauner, O.; Mao, H. K.; Hemley, R. J. P-V-T Equation of State of Platinum to 80 GPa and 1900 K from Internal Resistive Heating/X-Ray Diffraction Measurements. *J. Appl. Phys.* **2008**, *103* (5), 054908.
(72) Kalintsev, A.; Migdisov, A.; Alcorn, C.; Baker, J.; Brugger, J.; Mayanovic, R. A.; Akram, N.; Guo, X.; Xu, H.; Boukhalfa, H.; et al. Uranium Carbonate Complexes Demonstrate Drastic Decrease in Stability at Elevated Temperatures. *Commun. Chem.* **2021**, *4* (1), 120.
(73) Strzelecki, A. C.; Reece, M. E.; Zhao, X.; Yu, W.; Benmore, C. J.; Ren, Y.; Alcorn, C. D.; Migdisov, A.; Xu, H.; Guo, X. Thermodynamics of Mixing HREE in Xenotime Solid Solution ($Er_{(x)}Yb_{(1-x)}PO_4$). *ACS Earth Space Chem.* **2022**, *6*, 1375−1389.
(74) Klotz, S.; Chervin, J. C.; Munsch, P.; Le Marchand, G. Hydrostatic Limits of 11 Pressure Transmitting Media. *J. Phys. D. Appl. Phys.* **2009**, *42* (7), 075413.

https://doi.org/10.1021/acs.jpcc.2c06657
J. Phys. Chem. C XXXX, XXX, XXX−XXX

(75) Kamb, B. Structure of Ice VI. *Science (80-.).* **1965**, *150* (10), 205−209.
(76) Chen, J. Y.; Yoo, C. S. High Density Amorphous Ice at Room Temperature. *Proc. Natl. Acad. Sci. U. S. A.* **2011**, *108* (19), 7685−7688.
(77) Salzmann, C. G. Advances in the Experimental Exploration of Water's Phase Diagram. *J. Chem. Phys.* **2019**, *150* (6), 060901.
(78) Bina, C. R.; Navrotsky, A. Possible Presence of High-Pressure Ice in Cold Subducting Slabs. *Nature* **2000**, *408* (6814), 844−847.
(79) Gillet, P.; Malézieux, J. M.; Itié, J. P. Phase Changes and Amorphization of Zeolites at High Pressures: The Case of Scolecite and Mesolite. *Am. Mineral.* **1996**, *81* (5−6), 651−657.
(80) Zhu, J.; Quan, Z.; Lin, Y. S.; Jiang, Y. B.; Wang, Z.; Zhang, J.; Jin, C.; Zhao, Y.; Liu, Z.; Brinker, C. J.; Xu, H. Porous Ice Phases with VI and Distorted VII Structures Constrained in Nanoporous Silica. *Nano Lett.* **2014**, *14* (11), 6554−6558.
(81) Errandonea, D.; Garg, A. B. Recent Progress on the Characterization of the High-Pressure Behaviour of AVO_4 Orthovanadates. *Prog. Mater. Sci.* **2018**, *97* (April), 123−169.
(82) Dawson, P.; Hargreave, M. M.; Wilkinson, G. R. The Vibrational Spectrum of Zircon ($ZrSiO_4$). *J. Phys. C Solid State Phys.* **1971**, *4* (2), 240−256.
(83) Clavier, N.; Szenknect, S.; Costin, D. T.; Mesbah, A.; Poinssot, C.; Dacheux, N. From Thorite to Coffinite: A Spectroscopic Study of $Th_{1-X}U_xSiO4$ Solid Solutions. *Spectrochim. Acta - Part A Mol. Biomol. Spectrosc.* **2014**, *118*, 302−307.
(84) Kolesov, B. A.; Geiger, C. A.; Armbruster, T. The Dynamic Properties of Zircon Studied by Single-Crystal X-Ray Diffraction and Raman Spectroscopy. *Eur. J. Mineral.* **2001**, *13* (5), 939−948.
(85) Hoskin, P. W. O.; Rodgers, K. A. Raman Spectral Shift in the Isomorphous $(Zr_{1-X}Hf_x)$ SiO_4. *Eur. J. Solid State Inorg. Chem.* **1996**, *33* (11), 1111−1121.
(86) Nasdala, L. Spectroscopic Methods Applied to Zircon. *Rev. Mineral. Geochem.* **2003**, *53*, 427−467.
(87) Syme, R. W. G.; Lockwood, D. J.; Kerr, H. J. Raman Spectrum of Synthetic Zircon ($ZrSiO_4$) and Raman Spectrum of Synthetic Zircon ($ZrSiO_4$) and Thorite. *Solid State Phys.* **1977**, *10*, 1335−1348.
(88) Geisler, T.; Burakov, B. E.; Zirlin, V.; Nikolaeva, L.; Pöml, P. A Raman Spectroscopic Study of High-Uranium Zircon from the Chernobyl "Lava. *Eur. J. Mineral.* **2006**, *17* (6), 883−894.
(89) Manjón, F. J.; Errandonea, D.; Garro, N.; Pellicer-Porres, J.; Rodríguez-Hernández, P.; Radescu, S.; López-Solano, J.; Mujica, A.; Muñoz, A. Lattice Dynamics Study of Scheelite Tungstates under High Pressure I. $BaWO_4$. *Phys. Rev. B - Condens. Matter Mater. Phys.* **2006**, *74* (14), 1−17.
(90) Manjon, F. J.; Errandonea, D.; Garro, N.; Pellicer-Porres, J.; López-Solano, J.; Rodríguez-Hernández, P.; Radescu, S.; Mujica, A.; Muñoz, A. Lattice Dynamics Study of Scheelite Tungstates under High Pressure II. $PbWO_4$. *Phys. Rev. B - Condens. Matter Mater. Phys.* **2006**, *74* (14), 1−18.
(91) Kaur, H.; Sinha, M. M. Lattice Dynamical Investigations of Raman and Infrared Wavenumbers of Scheelite Structured Silicates. *Phys. B Condens. Matter* **2015**, *478*, 47−51.
(92) Smirnov, M. B.; Sukhomlinov, S. V.; Smirnov, K. S. Vibrational Spectrum of Reidite $ZrSiO_4$ from First Principles. *Phys. Rev. B - Condens. Matter Mater. Phys.* **2010**, *82* (9), 1−9.
(93) Gucsik, A. Micro-Raman Spectroscopy of Reidite as an Impact-Induced High Pressure Polymorph of Zircon: Experimental Investigation and Attempt to Application. *Acta Mineral.* **2006**, *47*, 17−24.
(94) Christofilos, D.; Papagelis, K.; Ves, S.; Kourouklis, G. A.; Raptis, C. High-Pressure Raman Study and Lattice Dynamical Calculations for $SrWO_4$. *J. Phys.: Condens. Matter* **2002**, *14* (47), 12641−12650.
(95) Christofilos, D.; Ves, S.; Kourouklis, G. A. Pressure Induced Phase Transitions in Alkaline Earth Tungstates. *Phys. Status Solidi B* **1996**, *198*, 539−544.
(96) Khanna, R. K.; Lippincott, E. R. Infrare Spectra of Some Scheelite Structures. *Spectrochim. Acta* **1968**, *24*, 905−908.
(97) Birch, F. Finite Strain Isotherm and Velocities for Single-Crystal and Polycrystalline NaCl at High Pressures and 300 K. *J. Geophys. Res.* **1978**, *83*, 1257.
(98) Gonzalez-Platas, J.; Alvaro, M.; Nestola, F.; Angel, R. EosFit7-GUI: A New Graphical User Interface for Equation of State Calculations, Analyses and Teaching. *J. Appl. Crystallogr.* **2016**, *49* (4), 1377−1382.
(99) Ehlers, A. M.; Zaffiro, G.; Angel, R. J.; Boffa-Ballaran, T.; Carpenter, M. A.; Alvaro, M.; Ross, N. L. Thermoelastic Properties of Zircon: Implications for Geothermobarometry. *Am. Mineral.* **2022**, *107* (1), 74−81.
(100) Angel, R. J. Equations of State. *Rev. Mineral. Geochemistry* **2000**, *41* (1), 35−59.
(101) Van Westrenen, W.; Frank, M. R.; Hanchar, J. M.; Fei, Y.; Finch, R. J.; Zha, C.-S. In Situ Determination of the Compressibility of Synthetic Pure Zircon ($ZrSiO_4$) and the Onset of the Zircon-Reidite Phase Transformation. *Am. Mineral.* **2004**, *89*, 197−203.
(102) Speer, J. A. The Actinide Orthosilicates. *Rev. Mineral. Geochem.* **1982**, *5*, 113−136.
(103) Marcial, J.; Zhang, Y.; Zhao, X.; Xu, H.; Mesbah, A.; Nienhuis, E. T.; Szenknect, S.; Neuefeind, J. C.; Lin, J.; Qi, L.; et al. Thermodynamic Non-Ideality and Disorder Heterogeneity in Actinide Silicate Solid Solutions. *npj Mater. Degrad.* **2021**, *5*, 34.
(104) Li, H.; Zhou, S.; Zhang, S. The Relationship between the Thermal Expansions and Structures of ABO_4 Oxides. *J. Solid State Chem.* **2007**, *180* (2), 589−595.
(105) Scott, H. P.; Williams, Q.; Knittle, E. Ultralow Compressibility Silicate without Highly Coordinated Silicon. *Phys. Rev. Lett.* **2001**, *88* (1), 015506.
(106) Hazen, R. M.; Finger, L. W.; Mariathasan, J. W. E. High-Pressure Crystal Chemistry of Scheelite-Type Tungstates and Molybdates. *J. Phys. Chem. Solids* **1985**, *46* (2), 253−263.
(107) Anderson, D. L.; Anderson, O. L. The Bulk Modulus-Volume Relationship for Oxides. *J. Geophys. Res.* **1970**, *75* (17), 3494−3500.
(108) Xu, H.; Zhao, Y.; Zhang, J.; Wang, Y.; Hickmott, D. D.; Daemen, L. L.; Hartl, M. A.; Wang, L. Anisotropic Elasticity of Jarosite: A High-P Synchrotron XRD Study. *Am. Mineral.* **2010**, *95* (1), 19−23.
(109) Hazen, R. M.; Finger, L. W. Bulk Modulus-Volume Rationship for Cation-Anion Polyhedra. *J. Geophys. Res.* **1979**, *84* (12), 6723−6728.
(110) Anderson, O. L.; Nafe, J. E. The Bulk Modulus-Volume Rationship for Oxide Compounds and Related Geophysical Problems. *J. Geophys. Res.* **1965**, *70* (16), 3951−3962.
(111) Hazen, R. M.; Downs, R. T.; Prewitt, C. T. Principles of Comparative Crystal Chemistry. *Rev. Mineral. Geochemistry* **2000**, *41* (1), 1−33.
(112) Crocombette, J. P.; Ghaleb, D. Modeling the Structure of Zircon ($ZrSiO_4$): Empirical Potentials, Ab Initio Electronic Structure. *J. Nucl. Mater.* **1998**, *257* (3), 282−286.
(113) Mondal, S. K.; Das, P. K.; Mandal, N.; Arya, A. A Novel Approach to the Structural Distortions of U/Th Snub-Disphenoids and Their Control on Zircon → Reidite Type Phase Transitions of $U_{1-X}Th_xSiO_4$. *J. Phys.: Condens. Matter* **2020**, *32* (14), 145401.
(114) Chaplot, S. L.; Pintschovius, L.; Choudhury, N.; Mittal, R. Phonon Dispersion Relations, Phase Transitions, and Thermodynamic Properties of $ZrSiO_4$: Inelastic Neutron Scattering Experiments, Shell Model, and First-Principles Calculations. *Phys. Rev. B - Condens. Matter Mater. Phys.* **2006**, *73* (9), 1−8.
(115) Mouri, T.; Enami, M. Raman Spectroscopic Study of Olivine-Group Minerals. *J. Mineral. Petrol. Sci.* **2008**, *103* (2), 100−104.
(116) Williams, Q.; Knittle, E.; Reichlin, R.; Martin, S.; Jeanloz, R. Structural and Electronic Properties of Fe_2SiO_4-Fayalite at Ultrahigh Pressures: Amorphization and Gap Closure. *J. Geophys. Res.* **1990**, *95* (B13), 21549−21563.
(117) Liu, L. G.; Mernagh, T. P. Raman Spectra of Forsterite and Fayalite at High Pressures and Room Temperature. *High Press. Res.* **1993**, *11* (5), 241−256.

https://doi.org/10.1021/acs.jpcc.2c06657
J. Phys. Chem. C XXXX, XXX, XXX−XXX

(118) Mernagh, T. P.; Liu, L.-G. Pressure Dependence of Raman Spectra from the Garnet End-Members Pyrope, Grossularite, and Almandite. *J. Raman Spectrosc.* **1990**, *21*, 305−309.
(119) Mulligan, S. R.; Stavrou, E.; Chariton, S.; Tschauner, O.; Salamat, A.; Wells, M. L.; Smith, A. G.; Hoisch, T. D.; Prakapenka, V. Equation of State for Natural Almandine, Spessartine, Pyrope Garnet: Implications for Quartz-in-Garnet Elastic Geobarometry. *Minerals* **2021**, *11* (5), 458.
(120) Mernagh, T. P.; Liu, L.-G. Raman Spectra from the Al_2SiO_5 Polymorphs at High Pressures and Room Temperature. *Phys. Chem. Miner.* **1991**, *18* (2), 126−130.

https://doi.org/10.1021/acs.jpcc.2c06657
J. Phys. Chem. C XXXX, XXX, XXX−XXX